

Characterization of Seismic Sources from Military Operations on Urban Terrain (MOUT): Examples from Baghdad

by Ghassan I. Aleqabi, Michael E. Wyssession, and Hafidh A. A. Ghalib

Abstract On 10 October 2006, a mortar attack on the U.S. Forward Operating Base Falcon, south of the Iraqi Capital Baghdad ammunition supply point, resulted in an ammunition “cook off” accompanied by numerous explosions. The explosions shook the base and damaged surrounding structures, and were both felt by Baghdadi residents and seismically recorded at the single broadband seismometer at the Baghdad seismic observatory BHD. The mortar activity, the ensuing explosions, and the accompanying military activities provided a wealth of information on the nature of seismic and acoustic wave generation and propagation resulting from nearby battlefield sources. Seismic records from the observatory show a variety of waveforms that can be qualified as different types of battlefield-related sources including mortars, tank ammunition, rockets, mines, and airborne vehicles. These different kinds of “military operations in urban terrain” are characterized and quantified by correlating their recorded military activity with observed seismic records and various aspects of the signals’ wave propagation.

Introduction

Most recent military conflicts have become increasingly urban and asymmetric in weaponry. The identification, characterization, and understanding of urban battlefield acoustic and seismic sources are important for military operations in urban terrain (MOUT). Generally, a wide variety of battlefield acoustics and seismic sources accompany MOUT, including different-caliber gunshots, artillery fire, mortar fire, shell impacts, explosions, helicopter transport, and the flight of unmanned Aerial Vehicles (UAVs, or “drones”). Understanding the seismic and acoustic sources and their wave propagations at scales of meters to kilometers has many military and forensic applications (e.g., Ottemöller and Evers, 2008).

During the fighting that has gone on in Baghdad, the BHD seismic station has recorded numerous events such as mortar blasts. The most clearly recorded events are those located close to BHD. Examples from closely detonated mortar rounds and a vehicle-borne improvised explosive device (VBIED) have been well-recorded. Figures 1-2 compare the seismic signals of mortar rounds and an improvised explosive device (IED) from the vertical component waveforms recorded at BHD, showing the different frequency characteristics of each.

Waveforms recorded during nearby mortar activity are shown in Figure 1a. For clarity, a shorter time segment is shown in Figure 1b. These waveforms were recorded at approximately 08:32 p.m. on 31 May 2006. Independent documentation on Iraqi civilian deaths from violence confirms the occurrence of mortar fire at this time (IBC, 2014,

incident k3149). The high-amplitude peaks on the trace are the airwaves that result from the firing of the mortar rounds. Of note are the similarity and repetitiveness of the waveforms, indicating similar sources. The energy is concentrated at higher frequencies, as demonstrated by the smoothed amplitude spectrum (Figure 1c), but the observed amplitude peak at 3 Hz is characteristic of mortar shell explosions.

Figure 2 shows waveforms from two VBIEDs. Their waveforms appear different, likely due to their different paths and different methods of detonation. Waveforms in Figure 2a are recorded at BHD at approximately 7:05 a.m. on 20 December 2006. For these kinds of sources, records on the timing, location, and type of military incident are available through various counter terrorism intelligence agencies. These sources (InteCenter, 2008; NCTC, 2008; IBC, 2014, incident k4937) reported that a suicide bomber drove his vehicle into a police checkpoint by the gate of Baghdad University. Figure 2c shows waveforms recorded at approximately 10:39 a.m. on 17 June 2006 (IBC, 2014, incident k3280). This incident was described as a car bomb targeting a police patrol in Al-Karradah, Baghdad (the BHD station is located within the Al-Karradah area).

The waveform for the nearby VBIED in Figure 2a is much simpler than the more complicated waveform for the VBIED in Figure 2c, which is farther from BHD, based on the IBC reports. The VBIED for the record in Figure 2a was detonated in a more open location than the one for the record in Figure 2c, which may also contribute the difference in the complexity of the signals (the VBIED for Figure 2c was detonated within a two-way road bordered by several-story buildings, which likely produced complex reverberations). The VBIED weapons vary in sizes and arming styles, though they generally consist of a motor vehicle (any size or type) filled with unexploded shells of

any caliber available in addition to an added explosive. Consequently, VBIED waveforms are generally complicated by the nature of the composite source and added signals from the destroyed targets and damage to the surrounding structures. Unfortunately, vehicle bombs are often the weapon of choice for terrorists, allowing large quantities of explosive to reach the intended target in a clandestine manner.

On October 10, 2006, mortar and/or rocket rounds fired by Iraqi insurgents destroyed the Forward Operating Base Falcon (FOBF) ammunition supply point (ASP) (Figure 3), located only about seven kilometers south of the Baghdad seismic observatory (Figure 4). This attack involved a series of explosions, lasting for hours, that rocked the base and were widely felt within Baghdad at the same time as being broadcast live on local TV channels and CNN News. Seismic signatures produced by the explosions and other related activities were digitally recorded at BHD (Figure 5). Media sources and the Pentagon reported that mortar and rocket attacks occurred in the late evening hours of the day.

At least one enemy mortar shell (Figure 5a) hit the ammunition depot and initiated an ammunition “cook off,” which is the premature firing of ammunition caused by unexpected heat within the environment. The initial major explosion occurred at 10:40 p.m. local time (19:40 GMT, Figure 5b)) and was followed by a series of explosions of varying sizes over the following hour (Figure 5c). Flashes and the appearance of mushroom-shaped clouds accompanied some of these explosions, which at the time led some local observers to erroneously presume nuclear weapons had been detonated.

This incident and its seismic recordings provided an opportunity to improve our ability to understand the generation and propagation of seismic waves from such an

unplanned incident. The diversity in explosion sources, containment conditions, and propagation environments within urban warfare conditions adds layers of complexity to the already challenging problem of the quantification and classification of manmade sources. Making interpretations even more difficult in this case is the lack of infrasound recordings from the explosions, preventing direct correlations of the acoustic energy released during explosion events with the recorded seismic energy.

Although the instruments at BHD recorded waveforms from MOUT sources, most of the observed parts of the MOUT sources are from the airwaves, with body wave signals often obscured by ambient noise and attenuation. Distinguishing the difference between MOUT signals caused by an IED and by mortar fire or heavy traffic is a challenging problem. To fully understand the differences between the waveforms of the various MOUT sources and distinguish between them requires a level of ground truth (exact times and explosive yields) that is not available in this case. However, significant insights into the nature of these MOUT sources can be gained by studying their frequency contents, time and frequency distributions, and propagation paths.

Data from the Baghdad Seismic Observatory (BHD)

As part of an on-going seismic deployment in Iraq (Ghalib *et al.*, 2006), the Baghdad Seismic Observatory was equipped with a broadband seismic station. The station consisted of a Streckeisen STS-2 seismometer and Quanterra Q330 acquisition system with Global Positioning System (GPS) timing, provided by the Incorporated Research Institutions for Seismology (IRIS) PASSCAL instrument center. The broadband data

were recorded at 100 samples per second. The seismic observatory in Baghdad was originally built in 1978, installed with a vault room containing an L-shaped concrete slab connected to the tops of three deep concrete columns.

Figure 5 shows three consecutive hours of vertical-component ground velocity recordings at station BHD, which is 7 km from the FOBF. The evening hour of 9 p.m. (local time) is marked by mortar and rocket-round activities (the peaks between 18:40 and 19:40 UTC in Figure 5a) that lead up to a major explosion at 10:40 p.m. (local time) (the peak at 19:40 UTC in Figure 5b), followed by numerous similar explosions (Figure 5c) continuing into the next day. Those explosions were initially audible up to several kilometers away from the FOBF, involving significant acoustic energy at frequencies of >20 Hz. The FOBF explosions were random in time, though with strikingly similar characteristics to one another. Preceding the explosion at 10:40 p.m., seismic records show impulsive sources (Figure 5a) that were most likely related to the mortar and rocket activities that triggered the 10:40 p.m. explosion. Visual reports suggest that these explosions ejected incandescent fragments, generated mushroom-shaped clouds, and were accompanied by large audible booms heard throughout Baghdad.

In addition to body waves, FOBF explosions perturbed the atmosphere, generating substantial energy in the infrasonic bandwidth (below 20 Hz) that arrived as atmosphere-to-ground direct airwaves (airblast). Seismograms from FOBF explosions contain an emergent P-wave onset, surface waves, and pronounced direct airwaves (Figure 6a and 6b). The direct arrivals of the airwaves are the strongest signals observed; their onsets are sharp and they are dominated by acoustic signals at frequencies >4 Hz. The generation and propagation of airwaves has been extensively studied (Press and Ewing, 1951;

Jardetzky and Press, 1952; Press and Oliver, 1955; Haskell, 1951; Mooney and Kaasa, 1962; Tanis, 1976; Alcudia and Stewart, 2007). The frequency content of the airwaves is shown in the Fourier spectral amplitude plot in Figure 6c. Most of the energy of the explosions is concentrated at 1-5 Hz, with peak seismic energy at ~ 5 Hz.

MOUT Acoustic-Seismic Partitioning

During a chemical explosion at or near Earth's surface, as with the FOBF MOUT explosions, the atmosphere is perturbed by the rapid release of energy that subsequently expands at supersonic velocities before reaching equilibrium with the surrounding air, generating non-linear shock waves. As the pressure waves radially expand, the Mach number decreases until they ultimately decay into acoustic airwaves that travel at ambient sound speeds (~ 340 m/s). As the airwave travels through the atmosphere, energy is continuously injected into the solid earth in the form of seismic waves. The physical properties of the air-surface interface determine the nature of the exchange of energy across the interface and therefore the nature of the propagating waves within both the atmosphere and ground. Recorded seismograms therefore involve a combination of seismic, ground-coupled, and infrasound energy.

Tanis (1976) described the two modes of coupling between airwaves and seismic waves. Acoustic airwaves can couple directly into the seismometer or the proximal ground area as a structural-borne sound. Airwaves may also continuously couple into the ground as they propagate along the surface at nearly grazing angles and frequencies with apparent seismic velocities that are very close to speed of sound in the air, exchanging

energy with existing surface waves that travel in the near-surface layer and generate air-coupled Rayleigh waves that propagate at the speed of sound. Local ground media influence the relative contributions of these two modes of coupling. For example, air-coupled Rayleigh waves will dominate if the layered structure of the ground supports the strong propagation of Rayleigh waves at these high frequencies (Tanis, 1976). Sound waves and seismic waves propagate with different group velocities and have different frequency contents; therefore the use of a multiple-filter analysis (MFT) will allow the identification and isolation of these waves.

In Figure 7, an MFT is applied to the seismic signal from the initial large explosion at FOBF in Figure 6a to identify the various wave types based on their dispersion characteristics. In this figure, dispersed surface waves as well as direct airwaves can be observed. Dispersion curves of the higher-mode Rayleigh wave (Figure 7b) and fundamental-mode Rayleigh wave (Figure 7c) are the most conspicuous. The ground-coupled surface waves (Figure 7d) arrive after the fundamental-mode Rayleigh waves and slightly resemble the fundamental-mode dispersion. An impulsive direct airwave arrival (Figure 7e) arrives at 0.35 km/s, followed immediately by the direct airwave packets (Figure 7f).

In Figure 8, a phase-match filter within the MFT is used to isolate the different waveforms. The initial large FOBF explosion (Figures 6a and 7) is analyzed at a set of distinct frequency bands that correspond to the various dispersion patterns. These include surface-waves, airwaves, and ground-coupled Rayleigh waves. Ground-coupled Rayleigh waves arrive slightly earlier than the acoustic waves. Direct airwaves are attached to ground-coupled Rayleigh waves, which are formed by the advancing shock front of the

direct airwaves as they move along the surface. Generally, it seems that near-surface explosions have significant levels of acoustic energy that couple with the atmosphere as well as to the ground. Unfortunately, with the lack of infrasound recording, air-coupled energy was not observed.

MOUT Sources and their Seismic Signatures

In identifying and classifying the sources of MOUT, we use several aspects of the seismic signals pertaining to the relative energy level of the signals, including the zero-crossing rates and time-frequency characteristics.

Impulsive sources such as chemical or nuclear explosions and artillery fire release energy over a broad spectral range that extends down to frequencies as low as 0.5 Hz and propagate large distances without significant attenuation. The signals of the different sources have differing characteristics. For example, mortar blasts produce both airwaves (generated during muzzle blasts and shell bursts) and body waves (generated from gun recoil and shell impacts) (Tanis, 1976). Mortar detonations (the firing of the mortar, as opposed to the blast of the explosion) are expected to excite energy at higher frequencies than the ensuing explosions, attributed to the short time duration of the confined muzzle blast.

Non-impulsive sources such as flying fighter jets, helicopters, and unmanned air vehicles (UAVs, or “drones”) produce seismic signals that display the harmonic oscillations from engines and/or rotors. These harmonics have frequencies ranging from several kHz down to 25 Hz or less. Movements of jet fighters, helicopters, and UAVs

toward or away from the receiver produce Doppler-shifted harmonics; examples of Doppler harmonics are seen in some of the records at BHD.

The signal processing methods considered for analysis are based on the frequency content of the MOUT signals. Generally, the frequency content of battlefield-related sources of interest span both the acoustic (> 20 Hz) and the infrasound (< 20 Hz) ranges. For similar source-receiver distances, underground seismic wave propagation undergoes significant attenuation in comparison to the airwaves propagating through the atmosphere. The resulting frequency-domain effects can be used to characterize MOUT sources. For time-domain characterization, analyses of seismic signal energy levels and zero-crossing rates can be used.

Short-term Energy and Zero-Crossing Rate (Time domain). The short-time energy (STE) and the short-time zero-crossing rate (STZCR) are widely used functions by the acoustic community to distinguish between voiced and unvoiced speech. The STZCR gives an approximate measure of the frequency content of a signal and can be used in conjunction with the STE (or magnitude) to discriminate between various MOUT sources. The STE and STZCR can show distinguishable features related to whether or not the signal is relatively rich in high-frequency content and can discriminate between mortars and other kinds of explosions.

The STE is an indication of the amplitude of the signal in the interval around time n that the analysis window is centered on, and is expressed as

$$E_n = \sum_{m=-\infty}^{\infty} x^2[m]w^2[n-m],$$

where $x[m]$ is the time series and $w[n]$ is the hamming window. The window slides

across a sequence of squared values, selecting intervals for processing.

The STZCR of a digitally sampled seismic signal is a measure of the number of times in a given time interval that the signal amplitude passes through a value of zero. It can be illustrated by:

$$Z_n = \frac{1}{2} \sum_{m=-\infty}^{\infty} |\text{sgn}\{x[m]\} - \text{sgn}\{x[m-1]\}|w[n-m],$$

where

$$\text{sgn}\{x[n]\} = \begin{cases} 1, & x[n] < 0 \\ -1, & x[n] \geq 0 \end{cases}$$

and $x[m]$ is the time series. The algebraic sign of $x[m]$ and $x[m-1]$ will determine whether Z_n is zero (same signs) or 1 (different signs).

Figures 9 and 10 demonstrate the identification of MOUT sources from STE and STZCR analyses by using two successive 15-minute time intervals. Both intervals precede the large explosion at 10:40 p.m. on 10 October 2006; one interval is of 19:22:00-19:37:00 UTC and the other is of 19:48:00-20:03:00 UTC.

Figure 9a shows bursts of activity during 19:22-19:24 that have relatively high zero-crossing rates (Figure 9b) and relatively low STE (Figure 9c), in comparison to the interval 19:26:30-19:27:00, which has low zero-crossing rates and comparatively high STE. Figure 10a, between 19:48 and 20:03, shows a series of signals that correspond to low STZCR (Figure 10b) and elevated STE signatures (Figure 10c). Also seen in Figure 10 is a low-energy signal at 20:01 that is associated with an elevated zero-crossing rate, indicating a non-impulsive source emitting high-frequency signals, likely due to the nearby passing of a helicopter. STE levels are significantly affected by the source energy;

explosions have a higher STE than mortar launches. However, mortars have a higher STZCR than explosions.

Time-Frequency Analysis. The time intervals in Figures 9 and 10 and the observed sources in those intervals can also be analyzed through time-frequency analysis, with spectrograms shown in Figures 11 and 12. Within the first five minutes of the interval in Figure 11 there appears high-frequency energy that is characterized by narrow vertical broadband signals. This energy corresponds to impulsive events that are probably related to mortar activity and may represent a combination of the Mach waves of the projectiles and waves from gun muzzles (Tanis, 1976). The energy peaks that are at ~ 2 Hz are probably related to the detonation of a high-energy projectile after its impact with the ground.

Two other noticeable signals are shown in Figure 11. One is a Doppler-shifted signal that starts at a frequency of 22 Hz and drops to 17 Hz by 19:32. The first overtone is more easily observed, which can be seen emerging at around 19:27:30 at 44 Hz and dropping to 34 Hz by 19:32. This Doppler-shifted signal is characteristic of the fly-by of an airborne vehicle such as a helicopter or drone. The other signal is from an undocumented explosion and has an energy peak of ~ 5 Hz at 19:36. This explosion likely played a significant role in the ammunition cook-off at FOFB that began about 4 minutes later, at 19:40. This is likely the blast at the ammunitions depot that led to the later on-site explosions.

The explosions in Figure 12 have a peak energy concentrated at ~ 5 Hz. At 20:01 there is a Doppler-shifted signal similar to what was seen about thirty minutes earlier (Figure 11). However, this signal corresponds to the high STZCR and low STE signal observed

in Figure 10. The dominant frequency shifts from about 12Hz to 9 Hz over about a half-minute corresponding to the maximum amplitudes in the spectrogram. This is explained by the engine and/or rotors of a moving airborne helicopter that changes direction and speed relative to the recording station as it passes by the station. Several overtones are also observed. The drop in frequency as the airborne vehicle passes can be used to determine the vehicle's speed ($= \Delta f / (2f_{\text{mean}})v_{\text{sound}}$). For the airborne vehicle in Figure 11, the speed is calculated to be ~110 mph, and the speed of the airborne vehicle in Figure 12 is calculated to be ~140. These values are appropriate for the cruising speeds of modern day combat helicopters.

Figure 13 shows the time period between Figures 11 and 12, when the main blast at the FOBF occurs, just after 19:40 UTC. This blast is significantly larger than any of the signals that arrive before it (note the difference in scale). There are a series of many smaller explosions that occur before the 19:40 blast, similar to one at 19:36 that was in Figure 11. It is likely that those small explosions first alerted the FOBF residents to seek safety and helped to trigger the ammunition cook-off that began with the major explosion of 19:40.

Figure 14 shows a set of large explosions that occurred within the hour following the 19:40 explosion. Some of these explosions released more energy than the 19:40 explosion. As the cook-off progressed, other well-contained large ammunitions began to explode. As with previous explosions, the peak energy of these events is concentrated at ~5 Hz.

Airwave Modeling. The determination of a shallow shear-wave velocity model is essential for characterizing explosion ground motion. The fundamental-mode Rayleigh

wave group-velocity dispersion curve (Figure 7c) was inverted for a plane-layered shallow shear-wave velocity model (Figure 15) using Herrmann and Ammon (2002). To gain insight into how the incorporation of an atmospheric layer into this model affects the synthetic seismogram, we computed synthetic seismograms (Figure 16), using a wave-number integration technique (Herrmann and Wang, 1985) for two cases, with and without a 40-km thick atmospheric layer. In Figure 16, for both cases, the synthetic seismograms of the fundamental-mode Rayleigh waves (Figures 16e and 16c) are comparable to the observed seismograms (Figure 16b and 16d). Adding an atmospheric layer and locating the explosion source above the ground surface incorporates airwave energy into the signals (Figure 16e). This arrival seems to arrive close in time to the ground-coupled Rayleigh waves (Figures 7d and 7e, and 8d and 8e) and modify their shape.

Explosion Source Characteristics

Determining the scaling laws that associate the amplitude-frequency spectrum of radiated energy with the seismic source size is important for seismic source characterization. The flat part of the spectrum at frequencies lower than the corner frequency is proportional to the source size (seismic moment). Infrasound records of airwaves from explosions can be used to estimate explosion sizes (Arrowsmith *et al.*, 2012; Keith *et al.*, 2002), but this is not straightforward for airwaves recorded on seismometers. The analysis here is therefore limited to estimating the source size from the broadband spectra of the P waves. This technique assumes that the low-frequency asymptote of the spectrum has the traditional

strong dependence on yield. For an explosion source, the spectrum can be modeled with the simple form

$$S(f) = \frac{S_o}{1 + \left(\frac{f}{f_c}\right)^\psi}$$

which is able to provide constraints on three parameters, S_o , f , and ψ . The low-frequency constant amplitude level, S_o , is proportional to the static displacement and is a measure of the seismic moment. The observed spectrum falls off beyond a corner frequency f_c at a rate of $f^{-\psi}$. We employed a three-parameter grid search to minimizing the root-mean-square error between observed and calculated spectra. The low-frequency spectral level

S_o is used to find the explosion moment M_o by

$$M_o = \frac{4\pi\rho\mathcal{R}S_o c^3}{0.6 * 2}$$

where ρ is the rock density at the source (kg/m^3), \mathcal{R} is the epicentral distance, and c is the P-wave velocity (m/s), while using the vertical-component displacement

seismogram (Havskov and Ottemöller, 2010). Values of c and ρ used in the calculation are $3400 m/s$ and $3000 kg/m^3$. Table 1 shows the corner frequencies, slopes, moments, and moment magnitude values of nine explosions, obtained through parameter grid searches. Included in the table are the corresponding TNT yield estimations using the formulation of Lahr (2000). Figure 17 shows examples of the root-mean-squares fits between the observed and modeled P-wave spectra for a VBIED source and an explosion (in this case, the explosion at 2006:283:19:40:09; Table 1).

Another technique for investigating explosions is to examine how frequency-band envelope functions, as defined by Oppenheim and Schafer (1989), vary with explosion

size (Stump *et al.*, 2003). Envelope functions based on Hilbert transforms are calculated for six different explosions from FOBF at variable frequency bands, which examine the explosion source frequency dependence. The envelope separation is used as a measure of scaling, called the scaling factor. The scaling factor for the different explosions was largest in the 4-8 Hz band, which is shown in Figure 18. This type of scaling was observed by Stump *et al.* (2003) for envelope functions from both contained and single-fired explosions. Path attenuation can cause frequency-dependent effects on the envelope amplitudes, but because in our case the propagation paths are similar, the observed scaling is most likely the result of frequency-dependent source-time functions (Mueller and Murphy, 1971).

Another approach in evaluating explosion sources is to determine their source-time functions, which reveals information about the physical mechanism and excitation process at the source of the explosion. A small and simple explosion can be used as a Green's function, representing path effects, so that when it is deconvolved from a larger and more complex event, the explosion source-time function is revealed (Ligorria and Ammon, 1999). This process assumes that the different events are co-located and have similar mechanisms, differing only in magnitude and duration.

Figure 19a shows the airwave arrivals from five different explosions, whose yield estimates are shown in Table 1. The small explosion (GF) is used as the empirical Green's function, to be deconvolved from the airwaves from four larger explosions (#1-4). Figures 19 b,c show relative source-time functions and their spectral amplitudes for the four larger explosions, displaying a well-defined attenuated impulse with subsequent energy release over the following several seconds. Based on the source time function,

relative differences between source amplitudes can be deduced. The largest of the four explosions is about 6 times larger than the smallest and larger than the other two nearly by a factor of two.

The calculated values presented in Table 1 do not take into account explosion source containment, which can play a significant role in size estimation. It is not publicly known what kind of ammunition was stored at the FOB site, and any explosions from bombs will have a different apparent yield than a standard chemical blast. The effect of the metallic casing of the shell and how it splinters can significantly affect the size estimation: the presence of a shell can reduce yield estimates, but shell splintering produces additional acoustic energy.

There are, in fact many possible sources of error when doing analysis with a single station; the explosions from FOBF were recorded at just one broadband seismic station (BHD). No additional equipment for recording infrasound or acoustic energy was available. This limited our capacity to locate sources and understand the nature of the wave generation and propagation, as well as the relative partitioning of energy between acoustic and seismic waves. The particular FOBF-to-BHD path geometry introduces a seismic characteristic that cannot be isolated without the availability of other stations. The same holds true for the other MOUT signals shown here. A number of assumptions are made in calculating the explosion sizes; for example, the explosion source models, radiation pattern corrections, geometrical spreading, and density and velocity structures could bias the estimations.

Conclusions

Detecting and characterizing seismic and acoustic sources from an urban battlefield can be a challenging problem. The 10 October 2006, FOBF explosions provided an excellent opportunity to study seismic signals from unplanned detonations, demonstrating a range of seismically observable characteristics. As the examples from the Baghdad station BHD show, there are a wide range of MOUT sources that all have characteristic seismic signatures. The spectral content of battlefield signals can provide information on source distance and type. Both time-domain and frequency-domain spectral techniques can take advantage of signal characteristics to differentiate between different kinds of stationary impulsive and non-impulsive moving sources. During mortar activity, the zero-crossing rate is relatively high compared to that of explosions. However, the short-time energy is relatively low for mortar signals compared to the seismic energy for explosions. The time-frequency representation is useful for distinguishing helicopter rotor noise as it has high zero-crossing rates and low short-time energy. Dispersion analysis shows that direct airwaves generate ground-coupled Rayleigh waves, formed by the transformation of direct airwaves on the ground that move along the surface at speeds comparable to air wave speeds.

Preliminary velocity analysis of the shallow structure using group velocity dispersion provided a model for validating phase arrivals in the observed data. P waves from FOBF explosions permitted the estimation of explosion sizes. FOBF explosions produce a linear increase in peak amplitude with explosive weight. Source scaling factors were observed to be strong for the 4-8 Hz pass band, but to show strong frequency dependence. The deconvolution of the empirical Green's function (obtained from a small explosion) from

the larger explosions illustrates that the air-wave source-time functions were similar, irrespective of size. For future studies, a co-located microphone and set of seismometers to record the air blast, ground-generated acoustic waves, and air-excited surface waves, including body and surface waves, would enhance our understanding of the wave phenomena associated with energy transfer at the air-ground interface, better enabling discrimination between seismic and coupled arrivals observed in the seismic time series, as well as the physical nature of the explosions. This type of research contributes to force protection, ammunition Depot management and engineering, and characterization of MOUT sources.

Data and Resources

Example:

The data used in this study is from the North Iraq Seismographic Network (NISN) operated by the Directorate General of Meteorology and Seismology, Kurdistan, Iraq. These data are not publicly available. The Computer Programs in Seismology V1.1.46 26 JUL 2013 were used, available at <http://www.eas.slu.edu/eqc/eqccps.html> (last accessed November 2013). Both the Seismic Analysis Code version 106.6, found at www.iris.edu/dms/nodes/dmc/software/downloads/sac/ (last accessed December 2013), and the SEIZMO Matlab toolbox, found at <http://epsc.wustl.edu/~ggeuler/codes/m/seizmo/> (last accessed July 2013), were used in processing and plotting seismic data.

Acknowledgments

The authors acknowledge the Directorate General of Meteorology and Seismology and their staff in Baghdad and Kurdistan region, Iraq. We would like to thank Robert B. Herrmann for making analysis programs available and for commenting on various aspects of an early version of this article, and Garrett Euler for making available the SEIZMO Matlab toolbox. The paper benefited from discussion with Brian Stump. Robert Wagner helped reformat the data.

References

- Alcudia, A. D., and R. R. Stewart (2007). Analysis of microphone and 3C geophone measurement from a 3C-2D seismic survey, *CREWES Research Report* **15**, no. 19, 1-20.
- Arrowsmith, S., R. Whitaker, J. MacCarthy, and D. Anderson (2012). A Sources-of-Error Model for Acoustic/Infrasonic Yield Estimation for Above-Ground Single-Point Explosions, *InfraMatics*, **1**, 1-9, doi: 10.4236/inframatics.2012.11001.
- Ghalib, H. A. A., G. I. Aleqabi, B. S. Ali, B. I. Saleh, D. S. Mahmood, I. N. Gupta, R. A. Wagner, P. J. Shore, A. Mahmood, S. Abdullah, O. K. Shaswar, F. Ibrahim, B. Ali, L. Omar, N. I. Aziz, N. H. Ahmed, A. A. Ali, A.-K. A. Taqi, and S. R. Khalaf (2006). Seismic characteristics of northern Iraq and surrounding regions, in *Proceedings of the 28th Seismic Research Review: Ground-Based Nuclear Explosion Monitoring Technologies LA-UR-06-5471*, **1**, pp. 40–48.
- Haskell, N. A. (1951). A note on air-coupled surface waves, *Bull. Seism. Soc. Am.* **41**, no. 4, 295-300.
- Havskov, J., and L. Ottemöller (2010). *Routine Data Processing in Earthquake Seismology*, Springer, Netherlands, 347 pp.
- Herrmann, R. B., and C. J. Ammon (2002). *Computer Programs in Seismology: Surface Waves, Receiver Functions and Crustal Structure*, Saint Louis University, Saint Louis, MO.
- Herrmann R. B., and C. Y. Wang (1985). A comparison of synthetic seismograms, *Bull. Seism. Soc. Am.*, **75**, no. 1, 41-56.

- IBC, Iraq body Count, 2014. URL <http://www.iraqbodycount.org/database/>.
- IntelCenter, 2008, Terrorism Incident Reference (TIR), Iraq (2006). Alexandria, VA, Tempest Publishing, LLC, 978-1606760154.
- Jardetzky, W. S., and F. Press (1952). Rayleigh-wave coupling to atmospheric compression waves, *Bull. Seism. Soc. Am.* **42**, 135-144.
- Le Pichon, A., J. Guilbert, A. Vega, A., M. Garcés, and N. Brachet (2001). Ground-coupled air waves and diffracted infrasound from the Arequipa earthquake of June 23, 2001, *Geophys. Res. Lett.* **29**, no. 18, 33-1 – 33-4.
- Ligorria, J. P., and C. J. Ammon (1999). Iterative deconvolution and receiver-function estimation, *Bull. Seism. Soc. Am.* **89**, 1395–1400.
- Mooney, H. M., and R. A. Kaasa (1962). Air waves in engineering seismology, *Geophys. Prosp.* **10**, 84-92.
- Mueller, C. S., and J. R. Murphy (1971). Seismic characteristics of underground nuclear detonations, Part I: Seismic spectrum scaling, *Bull. Seism. Soc. Am.* **61**, 1675-1692.
- National Counterterrorism Center (NCTC) (2007). *Report on Terrorist Incidents-2006*, 30 April 2007.
- Oppenheim, A. V., and R. W. Schaffer (1989). *Discrete-Time Signal Processing*, Prentice Hall, New York.
- Ottmøller, L., and L. G. Evers (2008). Seismo-acoustic analysis of the Buncefield oil depot explosion in the UK, 2005 December 11, *Geophys. J. Int.* **172**, 1123-1134.
- Press, F., and M. Ewing (1951). Ground roll coupling to atmospheric compressional waves, *Geophysics* **16**, 416-430.

- Press, F., and J. Oliver (1955). Model study of air-coupled surface waves: *J. Acoust. Soc. Am.* **27**, 43-46.
- Russell, D. W., R. B. Herrmann, and H. Hwang (1988). Application of frequency-variable filters to surface wave amplitude analysis, *Bull. Seism. Soc. Am.* **78**, 339-354.
- Stump, B. W., D. C. Pearson, and V. Hsu (2003). Source scaling of contained chemical explosions as constrained by regional seismograms, *Bull. Seism. Soc. Am.* **93**, 1212-1225.
- Tanis, F. J. (1976). Study of a Seismic Mortar Location Technique, CREWES Research Report, Environmental Research Inst of Michigan, Infrared and Optics Div.
- Vojinovic, D. (2006). [Online image],
<http://www.texansforpeace.org/endthewar/oldersoldiers6.htm> (AP Photo)
December 11, 2006.
- Zahradnik, J., and A. Plesinger (2010). Long-period pulses in broadband records of near earthquakes, *Bull. Seism. Soc. Am.* **95**, 1928-1939.

Department of Earth and Planetary Sciences

Washington University

St. Louis, MO 63130

ghassan@seismo.wustl.edu

(G.I.A., M.E.W.)

Advanced Technology Division

Array Information Technology

5130 Commercial Drive, Suite B

Melbourne, Florida 32940

(H.A.A.G.)

Table 1

Parameters for six military explosions.

Time (UTC) H:M:S	Corner Frequency f_c	Slope ψ	Moment M_o <i>dyne - cm</i>	Moment Magnitude M_w	TNT Tons	TNT Equivalent Tons
19:40:09 ¹	8.38	2.0	2.1695e+18	1.52	0.0029	0.194
20:05:07	8.14	2.68	4.3519e+18	1.72	0.0058	0.390
20:13:56	8.38	2.82	3.0702e+18	1.62	0.0041	0.275
20:31:22	8.14	2.68	4.3519e+18	1.72	0.0058	0.390
22:04:33	7.89	2.41	1.7165e+18	1.45	0.0023	0.153
2006.354.04.05.50*	11.08	2.0	2.0520e+18	1.50	0.0027	0.184

Results of a grid search of the optimal values of events parameters, based upon spectral amplitude analyses, for six explosions that occurred on October 10th, 2006, including one Vehicle Borne Improvised Explosive Device (VBIED) from 20 December 2006 (last row). We multiply the TNT ton by 1000/15 to account for the inefficiency of the TNT in generating seismic waves (Lahr, 1988).

Figure Captions

Figure 1. (a) Vertical-component 2-minute seismogram recorded at approximately 16:32 UTC, on 31 May 2006, illustrating mortar activities. (b) Segment of (a) showing the general character of the mortar rounds, which are very uniform. (c) and (d) Time series of the recording of a single mortar firing and its amplitude spectrum.

Figure 2. Example of vertical-component waveforms illustrating improvised explosion

devices. (a) Signal from a car bomb detonated close to BHD on 20 December 2006. (b) Amplitude spectrum of the waveform in (a). (c) Waveforms from another car bomb detonated on 17 June 2006 (note change in time scale from Figure 3a). (d) Amplitude spectrum of the waveform in (c). Note how the IED waveforms become more complicated with increased distance from BHD.

Figure 3. Photograph of the U.S. Forward Operation Base Falcon (FOBF) following the attack on 10 October 2006, showing damages sustained from both the enemy shelling and the ignition and “cook-off” of the ammunitions depot.

Figure 4. Map of Baghdad, Iraq, shows the locations of seismic station BHD and the FOBF.

Figure 5. Vertical-component waveforms recorded over a three-hour span between 18:00 and 21:00 UTC at BHD on 10 October 2006. All records use the same vertical scale. (a) Waveforms recorded at 9 p.m. (18:00 UTC) reveal mortar activities. (b) Waveforms recorded at 10 p.m. (19:00 UTC) show the first major explosion at FOBF with a peak at 19:40 UTC (10:40 p.m. local time), which was preceded and followed by smaller explosions. (c) Waveforms recorded at 11 p.m. (20:00 UTC) show multiple strong explosions at FOBF.

Figure 6. (a) Vertical, radial, and transverse components of waveforms from the first large explosion (10:40 p.m. local time, 19:40 UTC) recorded at BHD on 10 October

2006. (b) Stack of vertical-component waveforms from four different explosions. Large-amplitude airwaves arrive about 20 s after the origin time. (c) Amplitude spectrum of the stack shows a peak at roughly 5 Hz.

Figure 7. Result of MFT analysis applied to the waveform (a) of the vertical-component seismogram of the 2006:283:19:40 UTC explosion. Contour lines illustrate the amplitude of the signal envelope. At each frequency, four largest maxima of the envelope with squares, circles, triangles, and diamonds symbols are identified. A continuous sequence of the envelope maxima traces the dispersion curves. Curves (b) and (c) are higher and fundamental mode Rayleigh wave peaks that form the dispersion curves, (d) is the dispersed arrival, identified as ground-coupled surface-waves, (e) is the direct non-dispersive low frequency airwave, and (f) are the higher frequency airwave arrivals. Waveforms of (b), (c), (d), (e), and (f) are shown in Figure 8.

Figure 8. Illustration of the various types of arrivals that comprise an FOBF explosion waveform, including surface-waves, ground-coupled waves, and airwaves (Figure 7). Numbers on the right are the peak amplitudes of each wave type; notice that the ground-coupled surface-wave has the smallest peak amplitude. (a) Waveform of the vertical-component seismogram of the 2006:283:19:40 UTC explosion. (b) Isolated higher mode waveform. (c) Isolated fundamental mode waveform. (d) Isolated ground-coupled surface-wave waveform. (e) Isolated direct non-dispersive low frequency airwave waveform. (f) Isolated high-frequency direct airwaves.

Figure 9. (a) Vertical-component ground motion time series between 19:22:00 and 19:37:00 UTC (22:22 and 22:37 local time) recorded on 10 October 2006. (b) Short-time zero crossing rate, and (c) short-time energy for the time window in (a). The waveform just after 19:15 is an explosion at FOBF, and it is characterized by a low short-time zero-crossing rate but a high short-time energy. The large signal just before 19:25 is likely to be a mortar, characterized by both high zero-crossing rate and high short-time energy.

Figure 10. (a) Vertical-component ground motion time series between 19:48:00 and 20:03:00 UTC (22:48 and 23:03 local time) recorded on 10 October 2006. (b), (c) Short-time zero crossing rate, and short-time energy, respectively for the time window in (a). The signal ~19:37 has an anomalously high short-time zero crossing rate but low short-time energy, which is characteristic of a helicopter emitting high-frequency energy.

Figure 11. (top) Vertical-component seismogram for the time window between ~19:22:00 and 19:37:00 UTC, for 10 October 2006, the same time period for Figure 9. (bottom) Corresponding spectrogram. A variety of signals are shown that are probably produced by mortar activity, projectile detonation, explosions, and airborne vehicles. High-intensity energy at frequencies of > 8 Hz is indicative of mortar activity; energy at 5 Hz corresponds to explosions, energy of 1 - 3 Hz is related to projectiles, and the continuous bands that start high at > 22 Hz (with an overtone at 44 Hz) at about 19:31 and drop low to ~ 16 Hz after $\sim 19:32$ show the characteristic Doppler shift seen in flying helicopters and other airborne vehicles. The spectrogram is the power spectral density (PSD) in decibels normalized so that 0 dB is the maximum.

Figure 12. (a) Vertical-component seismogram for the time window between ~19:48 and 20:03 UTC, for 10 October 2006, the same time period as Figure 10. (b) Corresponding spectrogram. High-intensity energy at ~5 Hz is related to explosions. As with Figure 11, this record shows a Doppler-shifted signal (at ~20:00-20:02) that is likely associated with a flying projectile or helicopter. In this case the dominant frequency is ~12 Hz, with three overtones observed at ~24 Hz, 36 Hz, and 48 Hz (just the lower-frequency tail of the highest of these overtones is observed).

Figure 13. (a) Vertical-component ground motion time series between 19:35:00 and 19:45:00 UTC (22:35 and 22:45 local time) recorded on 10 October 2006. (b), (c) Short-time zero-crossing rate, and short-time energy, respectively for the time window in (a). The signal ~19:37 has an anomalously high short-time zero crossing rate but low short-time energy, which is characteristic of a helicopter emitting high-frequency energy, while signal at 19:40 has low short-time zero crossing rate but high short term energy, which indicates an impulsive source, (d) Corresponding spectrogram. A variety of signals are shown that were produced by FOBF explosion. The high-intensity energy at frequencies of ~5 Hz is related to explosions, with both body waves and airwaves visible for the explosion in addition to Doppler effect signal ~19:37.

Figure 14. (a) A time window between ~20:13:00 and 20:28:00 UTC of vertical-component waveforms recorded on 10 October 2006. (b) Corresponding spectrogram. A variety of signals are shown that were produced by FOBF explosions. The high-intensity

energy at frequencies of ~ 5 Hz is related to explosions, with both body waves and airwaves visible for each explosion.

Figure 15. S- and P-wave velocity models for the structure between FOBF and BHD, including an atmosphere, obtained from inverting fundamental-mode Rayleigh waves and used in generating synthetic seismograms.

Figure 16. Various types of waves that comprise the explosion waveforms and a comparison with explosion synthetic seismograms with and without an atmospheric layer. (a) Vertical-component seismogram of the 2006:283:19:40 UTC explosion. (b) Isolated fundamental mode waveform. (c) Synthetic seismogram using a velocity model without an atmospheric layer. (d) Isolated airwave waveform. (f) Synthetic seismogram using a velocity model with atmospheric layer; note the presence of airwaves about ~ 22 minutes after the origin.

Figure 17. (a) Example of vertical-component displacement amplitude spectra for both a VBIED explosion at 04:06 UTC on 10 October 2006 (crosses), and the best fitting spectral model (solid line). (b) Similar example for the large ammunition explosion at 19:40 UTC, 10 October 2006.

Figure 18. Smoothed envelope functions for 6 different explosions of differing sizes, displayed at the frequency band-pass of 4-8 Hz.

Figure 19. (a) Vertical-component seismograms of airwaves from 5 different explosions (details are given in Table 1). Seismograms are sorted by amplitude. The smallest signal (bottom) is selected as an empirical Green's function. (b) Estimated source-time functions for the the 4 explosions in (a) obtained by deconvolving out the Green's function. Because all of the source-time functions in (b) involve a small, wide pulse ~ 1.9 s after the main pulse, it is likely that this signal is not present in the assumed Green's function (bottom). (c) Amplitude spectra of the four source-time functions show difference in energy is at maximum at the low frequency region. At the higher frequencies above 5 Hz the difference is less because of the rapid high-frequency attenuation.

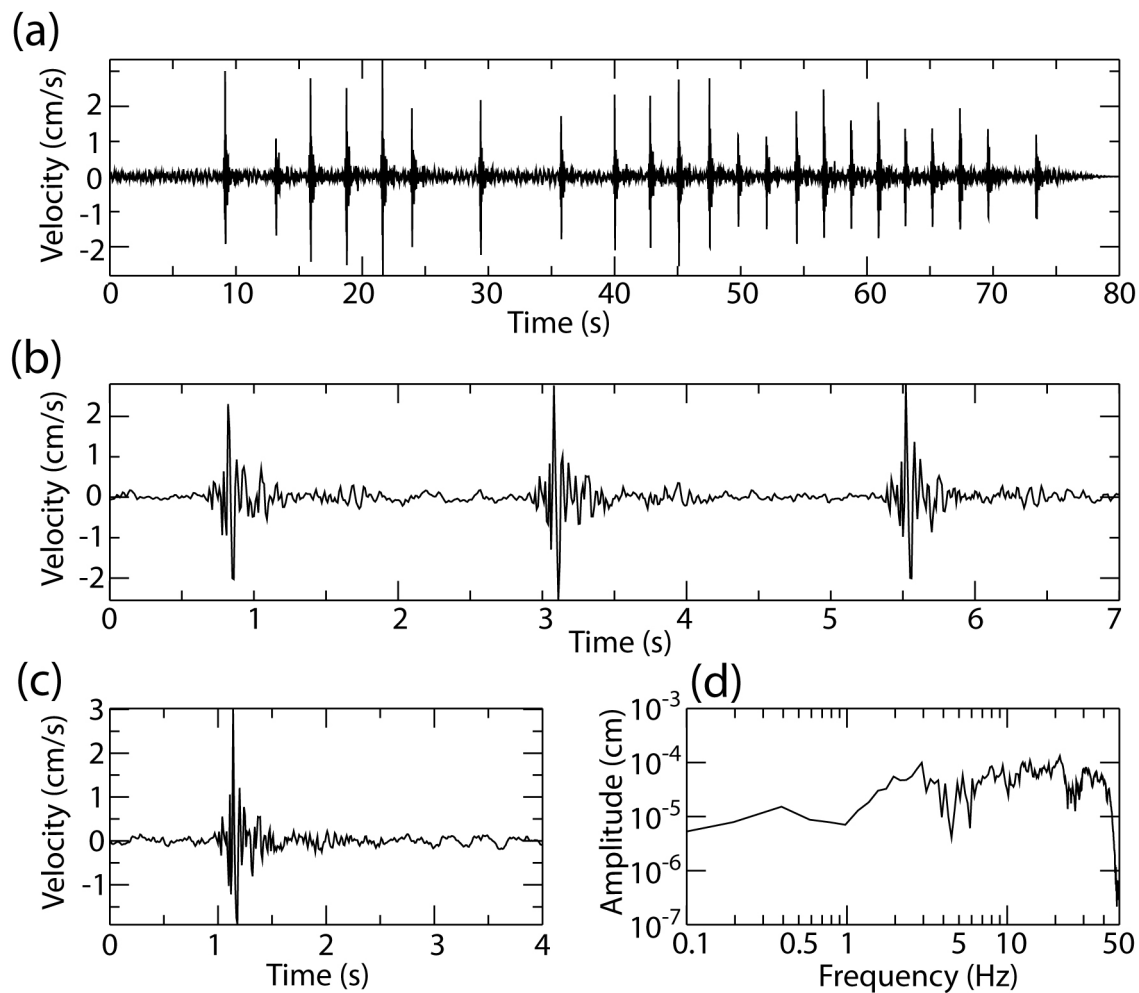


Figure 1. (a) Vertical-component 2-minute seismogram recorded at approximately 16:32 UTC, on 31 May 2006, illustrating mortar activities. (b) Segment of (a) showing the general character of the mortar rounds, which are very uniform. (c) and (d) Time series of the recording of a single mortar firing and its amplitude spectrum.

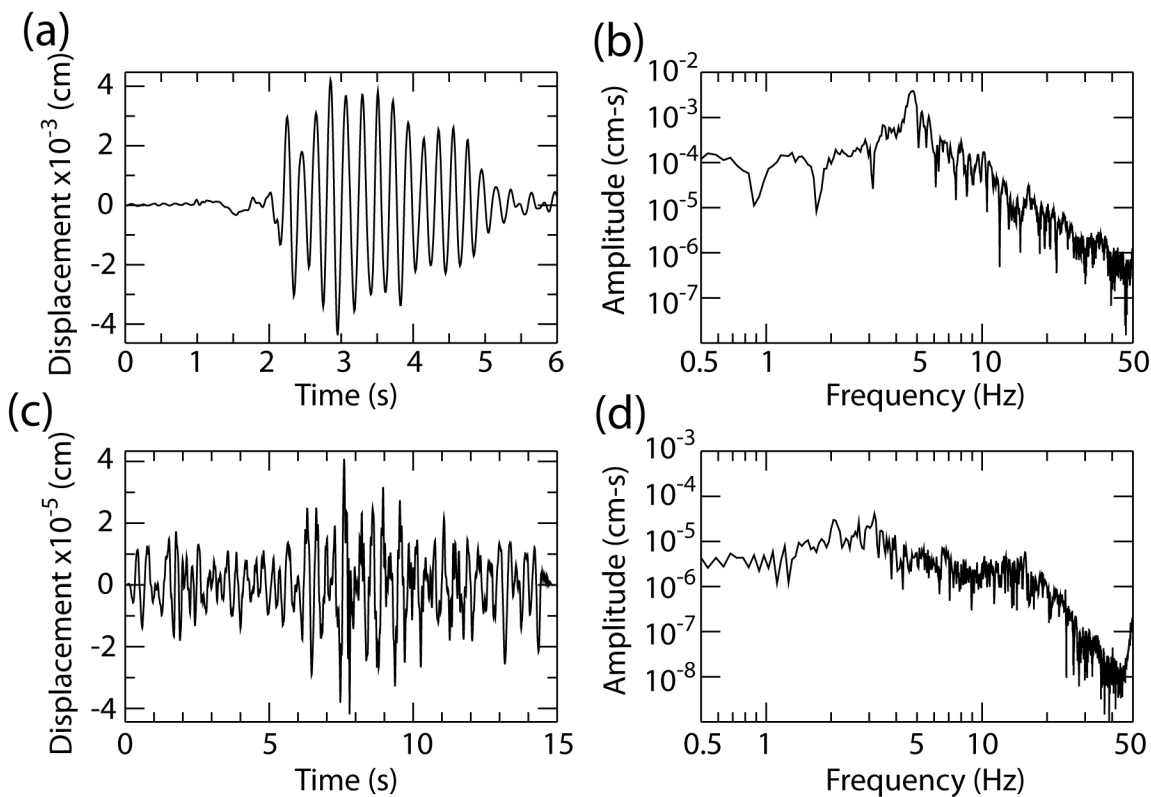


Figure 2. Example of vertical-component waveforms illustrating improvised explosion devices. (a) Signal from a car bomb detonated close to BHD on 20 December 2006. (b) Amplitude spectrum of the waveform in (a). (c) Waveforms from another car bomb detonated on 17 June 2006 (note change in time scale from Figure 3a). (d) Amplitude spectrum of the waveform in (c). Note how the IED waveforms become more complicated with increased distance from BHD.



Figure 3. Photograph of the U.S. Forward Operation Base Falcon (FOBF) following the attack on 10 October 2006, showing damages sustained from both the enemy shelling and the ignition and “cook-off” of the ammunitions depot.



Figure 4. Map of Baghdad, Iraq, shows the locations of seismic station BHD and the FOBF.

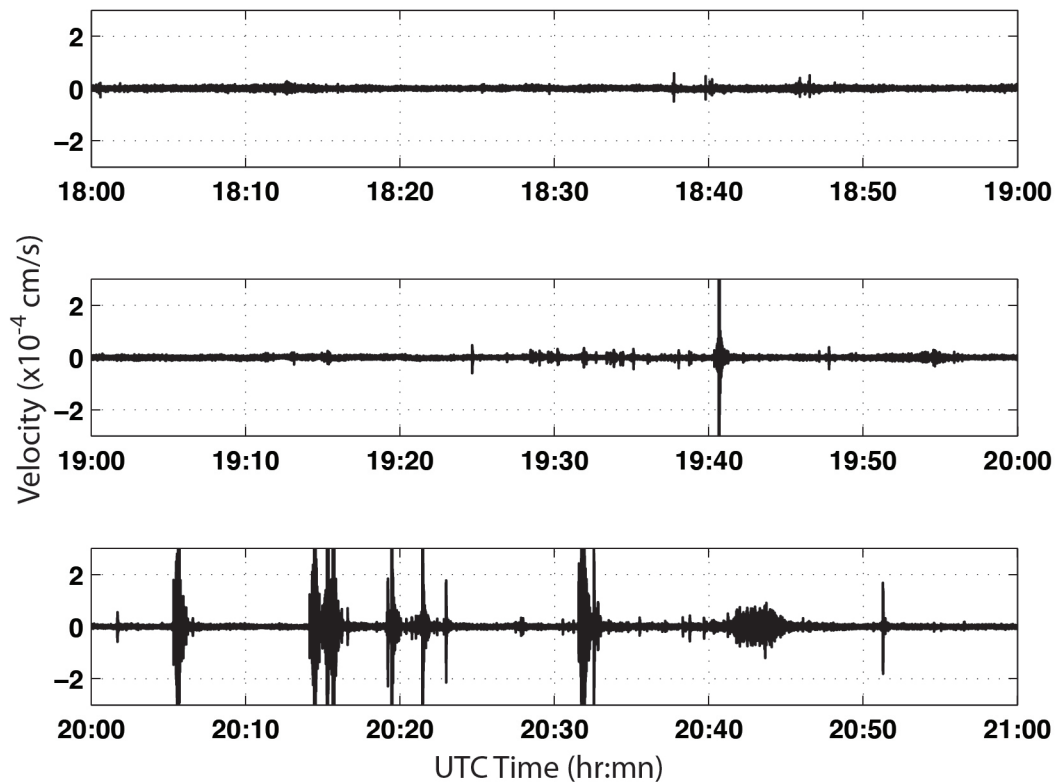


Figure 5. Vertical-component waveforms recorded over a three-hour span between 18:00 and 21:00 UTC at BHD on 10 October 2006. All records use the same vertical scale. (a) Waveforms recorded at 9 p.m. (18:00 UTC) reveal mortar activities. (b) Waveforms recorded at 10 p.m. (19:00 UTC) show the first major explosion at FOBF with a peak at 19:40 UTC (10:40 p.m. local time), which was preceded and followed by smaller explosions. (c) Waveforms recorded at 11 p.m. (20:00 UTC) show multiple strong explosions at FOBF.

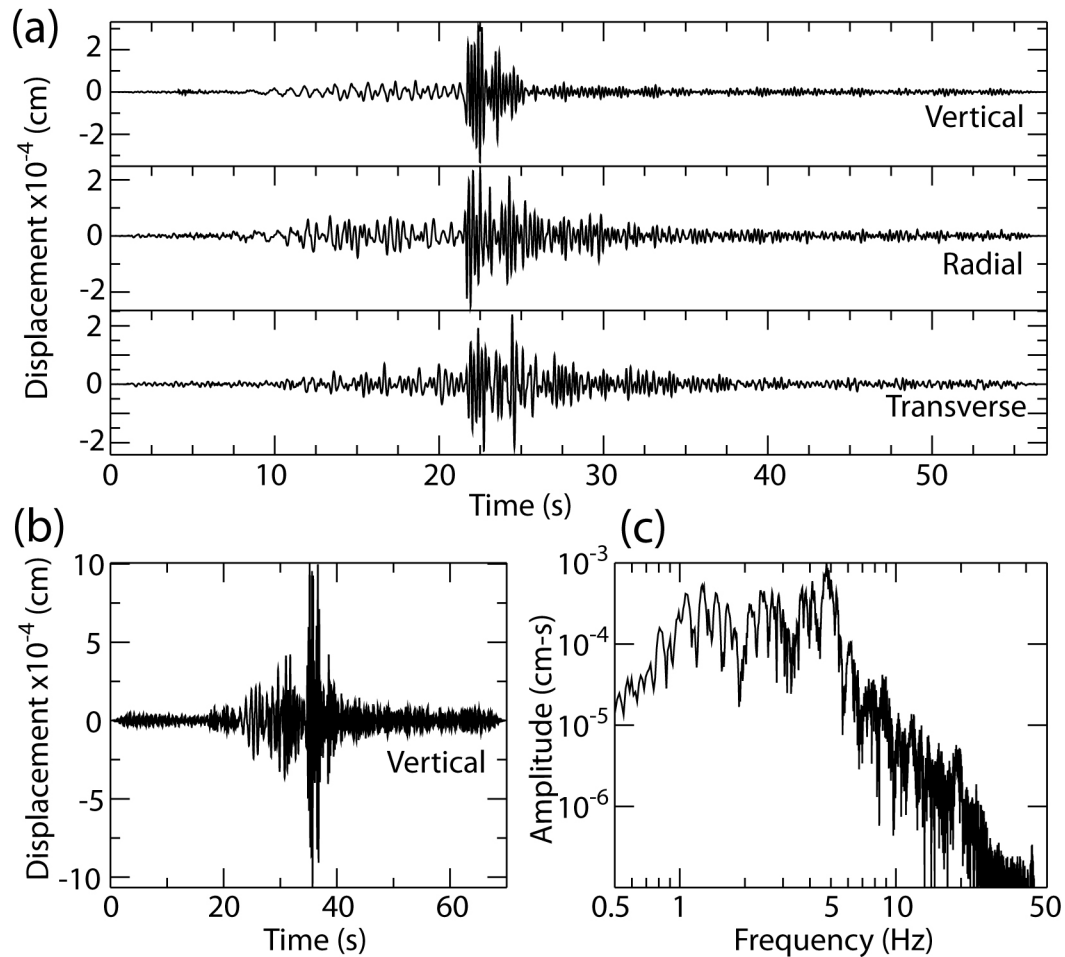


Figure 6. (a) Vertical, radial, and transverse components of waveforms from the first large explosion (10:40 p.m. local time, 19:40 UTC) recorded at BHD on 10 October 2006. (b) Stack of vertical-component waveforms from four different explosions. Large-amplitude airwaves arrive about 20 s after the origin time. (c) Amplitude spectrum of the stack shows a peak at roughly 5 Hz.

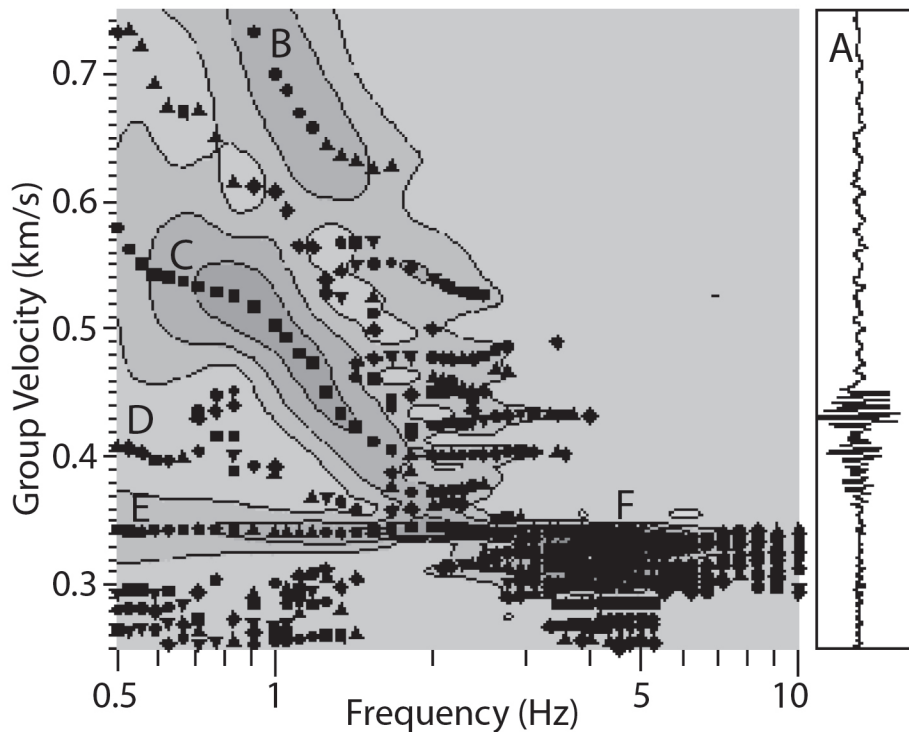


Figure 7. Result of MFT analysis applied to the waveform (a) of the vertical-component seismogram of the 2006:283:19:40 UTC explosion. Contour lines illustrate the amplitude of the signal envelope. At each frequency, four largest maxima of the envelope with squares, circles, triangles, and diamonds symbols are identified. A continuous sequence of the envelope maxima traces the dispersion curves. Curves (b) and (c) are higher and fundamental mode Rayleigh wave peaks that form the dispersion curves, (d) is the dispersed arrival, identified as ground-coupled surface-waves, (e) is the direct non-dispersive low frequency airwave, and (f) are the higher frequency airwave arrivals. Waveforms of (b), (c), (d), (e), and (f) are shown in Figure 8.

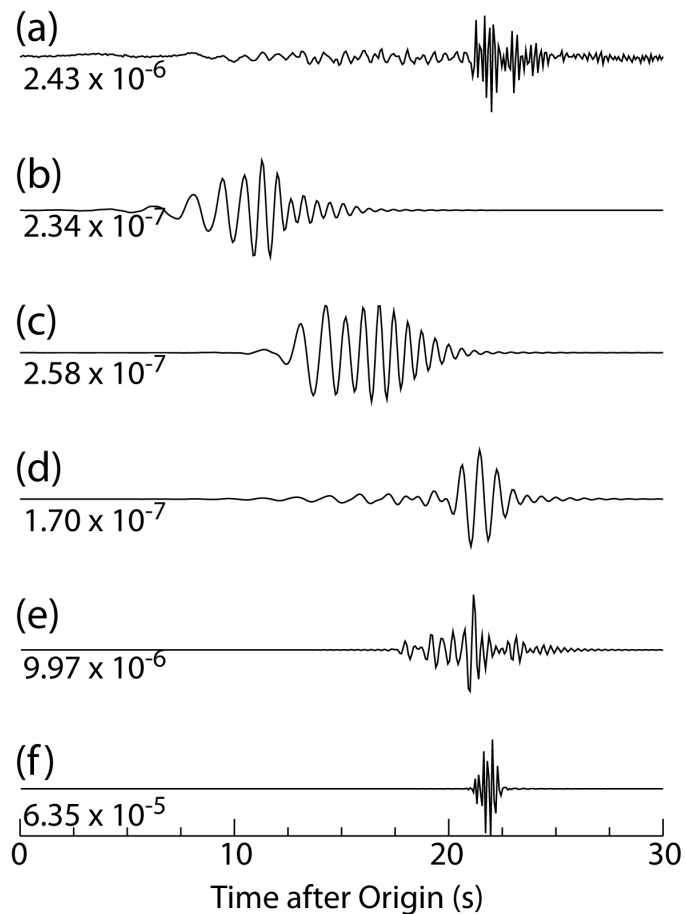


Figure 8. Illustration of the various types of arrivals that comprise an FOBF explosion waveform, including surface-waves, ground-coupled waves, and airwaves (Figure 7). Numbers on the right are the peak amplitudes of each wave type; notice that the ground-coupled surface-wave has the smallest peak amplitude. (a) Waveform of the vertical-component seismogram of the 2006:283:19:40 UTC explosion. (b) Isolated higher mode waveform. (c) Isolated fundamental mode waveform. (d) Isolated ground-coupled surface-wave waveform. (e) Isolated direct non-dispersive low frequency airwave waveform. (f) Isolated high-frequency direct airwaves.

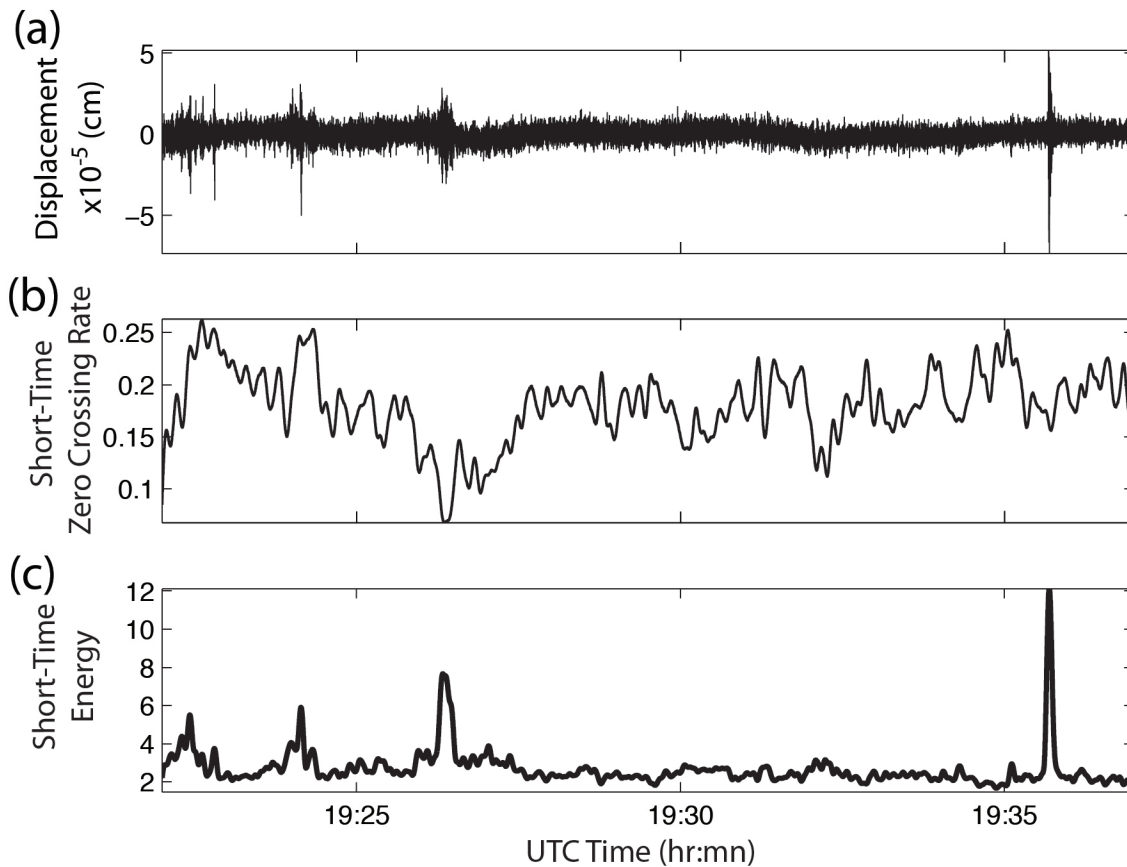


Figure 9. (a) Vertical-component ground motion time series between 19:22:00 and 19:37:00 UTC (22:22 and 22:37 local time) recorded on 10 October 2006. (b) Short-time zero crossing rate, and (c) short-time energy for the time window in (a). The waveform just after 19:15 is an explosion at FOBF, and it is characterized by a low short-time zero-crossing rate but a high short-time energy. The large signal just before 19:25 is likely to be a mortar, characterized by both high zero-crossing rate and high short-time energy.

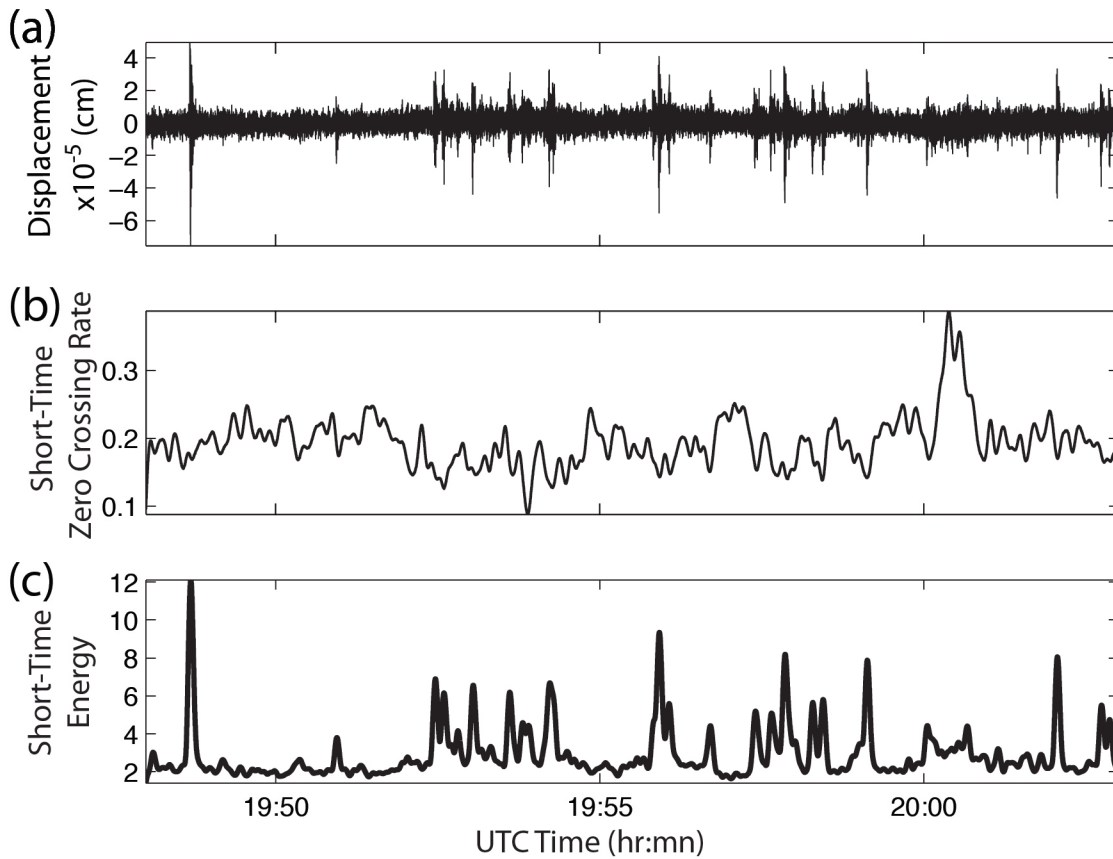


Figure 10. (a) Vertical-component ground motion time series between 19:48:00 and 20:03:00 UTC (22:48 and 23:03 local time) recorded on 10 October 2006. (b), (c) Short-time zero crossing rate, and short-time energy, respectively for the time window in (a). The signal $\sim 19:37$ has an anomalously high short-time zero crossing rate but low short-time energy, which is characteristic of a helicopter emitting high-frequency energy.

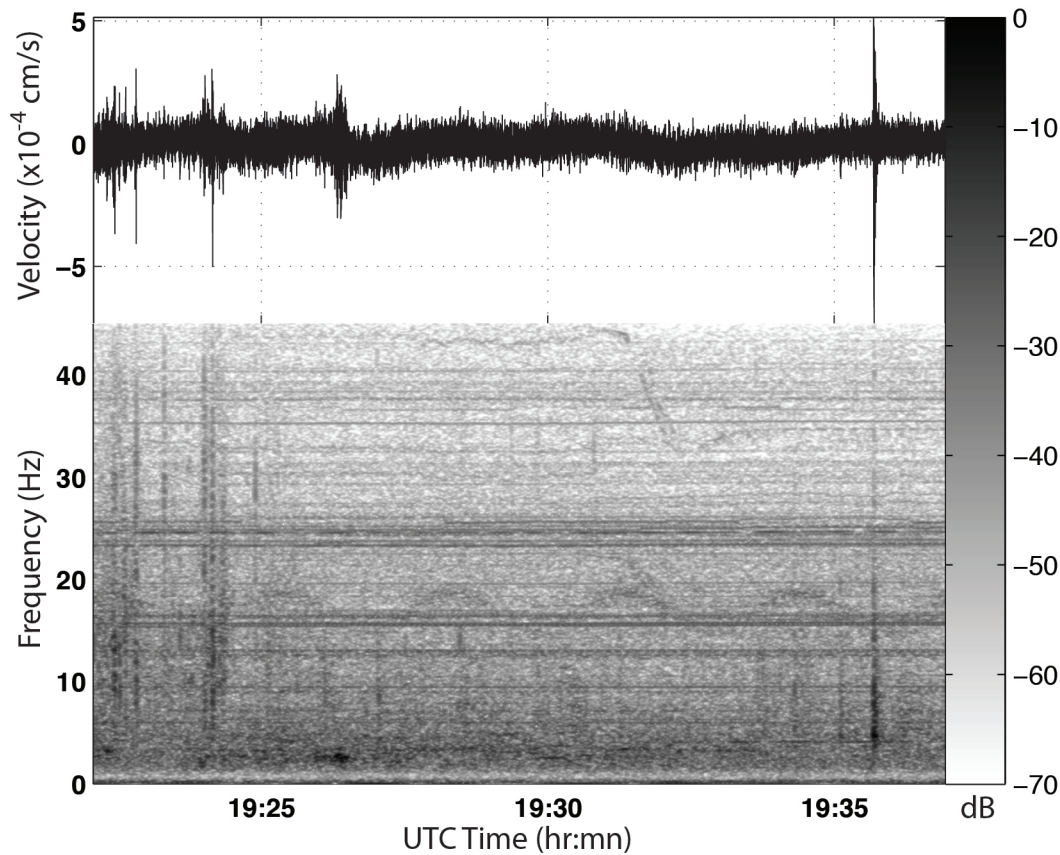


Figure 11. (top) Vertical-component seismogram for the time window between ~19:22:00 and 19:37:00 UTC, for 10 October 2006, the same time period for Figure 9. (bottom) Corresponding spectrogram. A variety of signals are shown that are probably produced by mortar activity, projectile detonation, explosions, and airborne vehicles. High-intensity energy at frequencies of > 8 Hz is indicative of mortar activity; energy at 5 Hz corresponds to explosions, energy of 1 - 3 Hz is related to projectiles, and the continuous bands that start high at > 22 Hz (with an overtone at 44 Hz) at about 19:31 and drop low to ~ 16 Hz after $\sim 19:32$ show the characteristic Doppler shift seen in flying helicopters and other airborne vehicles. The spectrogram is the power spectral density (PSD) in decibels normalized so that 0 dB is the maximum.

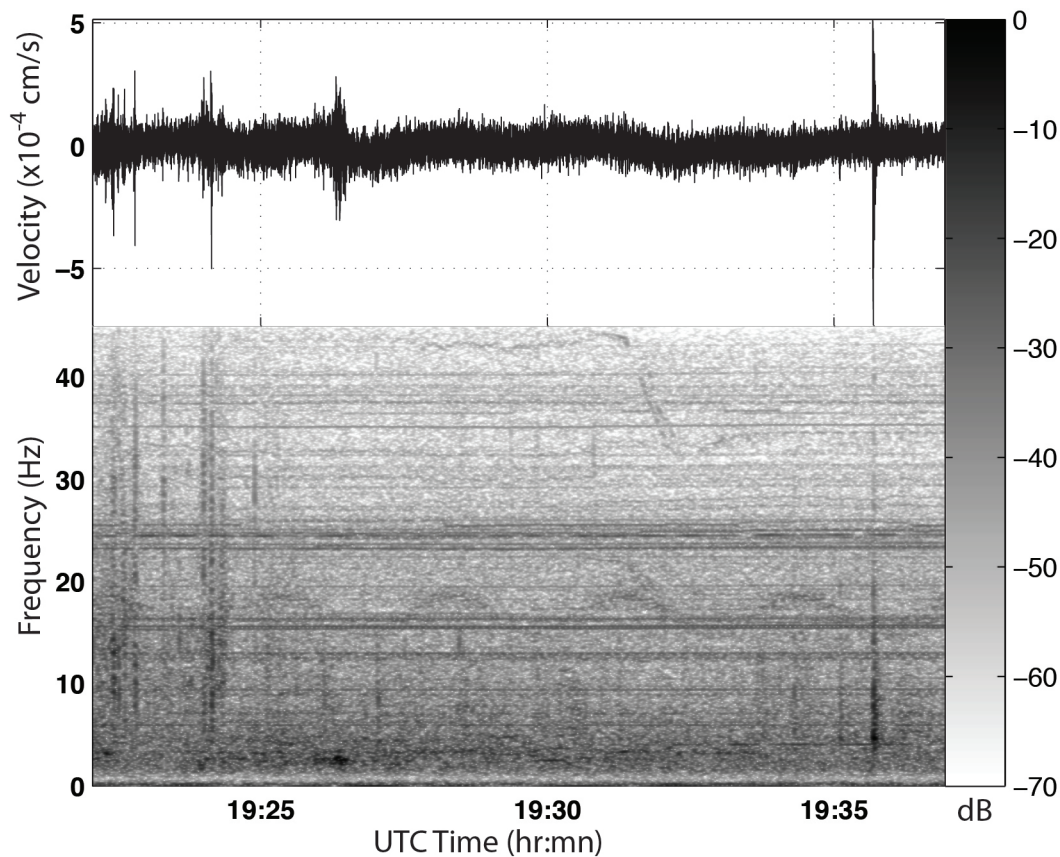


Figure 12. (a) Vertical-component seismogram for the time window between $\sim 19:48$ and 20:03 UTC, for 10 October 2006, the same time period as Figure 10. (b) Corresponding spectrogram. High-intensity energy at ~ 5 Hz is related to explosions. As with Figure 11, this record shows a Doppler-shifted signal (at $\sim 20:00$ -20:02) that is likely associated with a flying projectile or helicopter. In this case the dominant frequency is ~ 12 Hz, with three overtones observed at ~ 24 Hz, 36 Hz, and 48 Hz (just the lower-frequency tail of the highest of these overtones is observed).

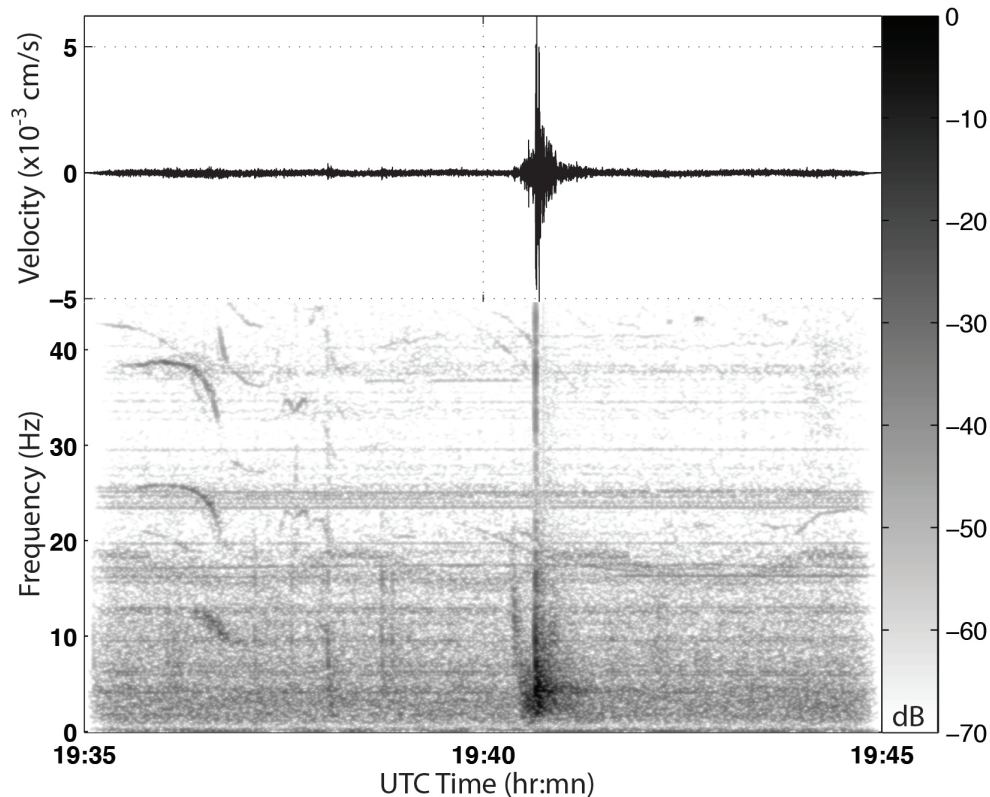


Figure 13. (a) Vertical-component ground motion time series between 19:35:00 and 19:45:00 UTC (22:35 and 22:45 local time) recorded on 10 October 2006. (b), (c) Short-time zero-crossing rate, and short-time energy, respectively for the time window in (a). The signal $\sim 19:37$ has an anomalously high short-time zero crossing rate but low short-time energy, which is characteristic of a helicopter emitting high-frequency energy, while signal at 19:40 has low short-time zero crossing rate but high short term energy, which indicates an impulsive source, (d) Corresponding spectrogram. A variety of signals are shown that were produced by FOBF explosion. The high-intensity energy at frequencies of ~ 5 Hz is related to explosions, with both body waves and airwaves visible for the explosion in addition to Doppler effect signal $\sim 19:37$.

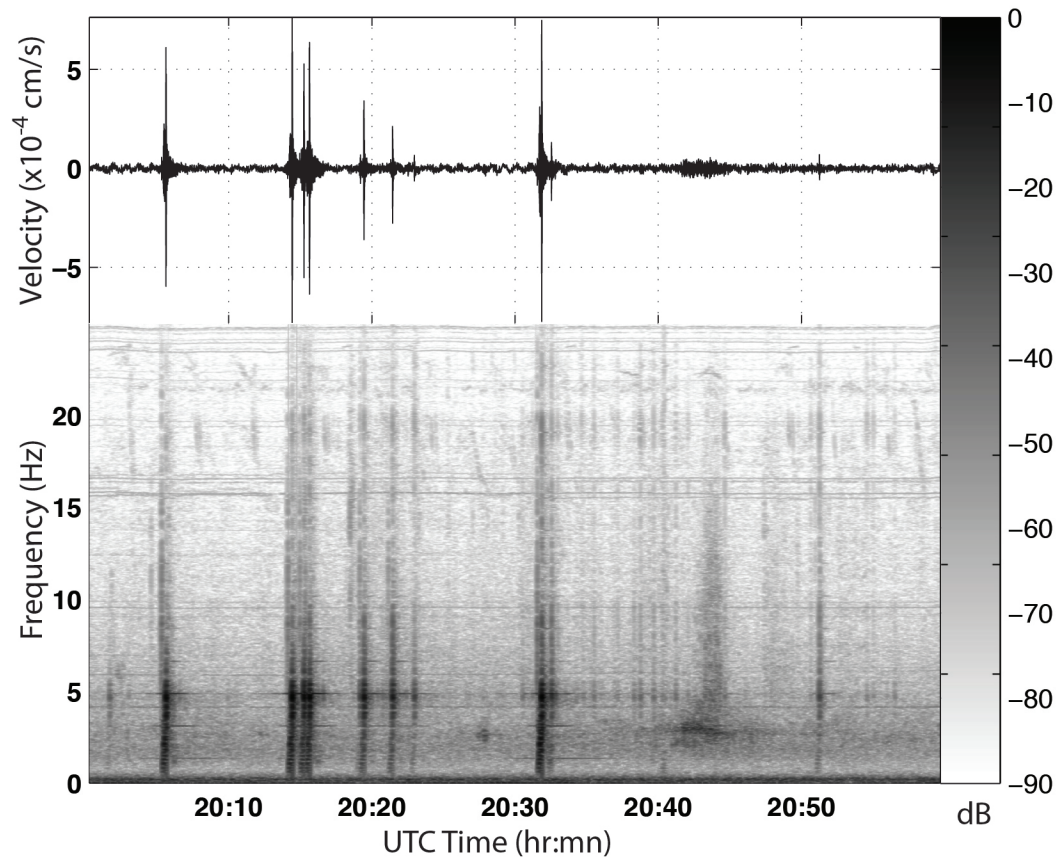


Figure 14. (a) A time window between $\sim 20:13:00$ and $20:28:00$ UTC of vertical-component waveforms recorded on 10 October 2006. (b) Corresponding spectrogram. A variety of signals are shown that were produced by FOBF explosions. The high-intensity energy at frequencies of ~ 5 Hz is related to explosions, with both body waves and airwaves visible for each explosion.

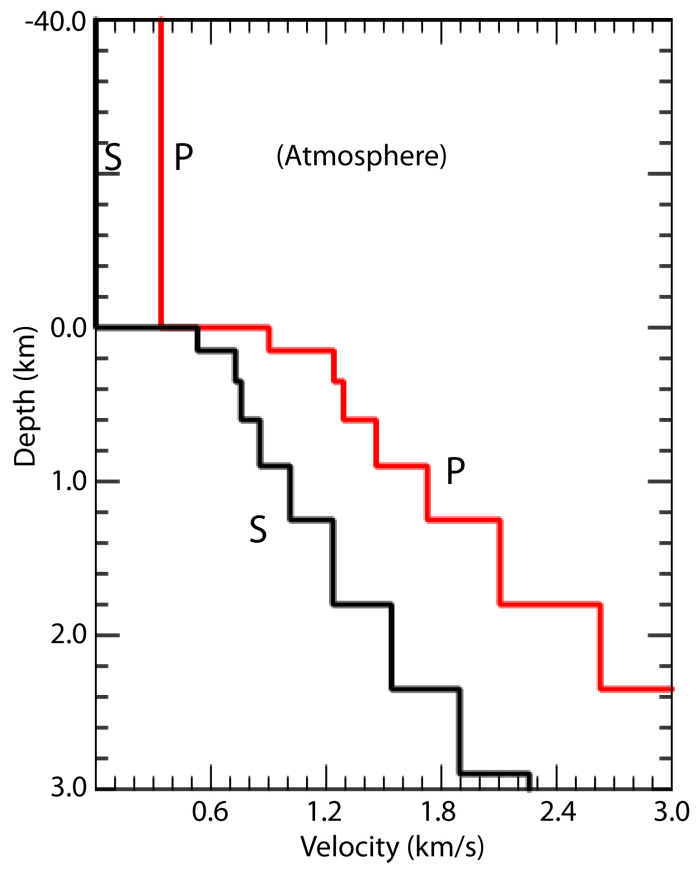


Figure 15. S- and P-wave velocity models for the structure between FOBF and BHD, including an atmosphere, obtained from inverting fundamental-mode Rayleigh waves and used in generating synthetic seismograms.

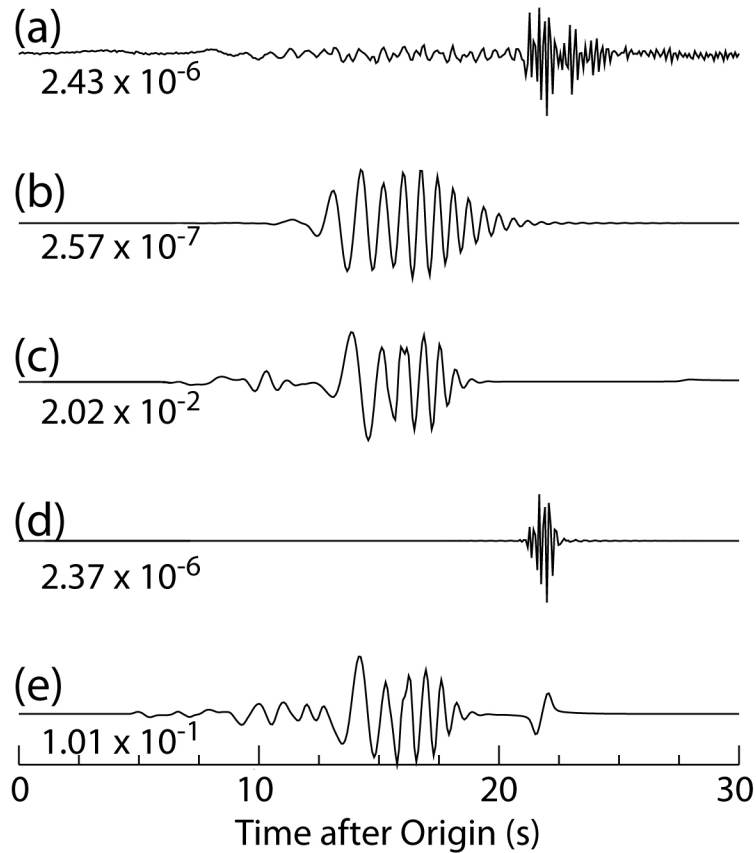


Figure 16. Various types of waves that comprise the explosion waveforms and a comparison with explosion synthetic seismograms with and without an atmospheric layer. (a) Vertical-component seismogram of the 2006:283:19:40 UTC explosion. (b) Isolated fundamental mode waveform. (c) Synthetic seismogram using a velocity model without an atmospheric layer. (d) Isolated airwave waveform. (f) Synthetic seismogram using a velocity model with atmospheric layer; note the presence of airwaves about ~22 minutes after the origin.

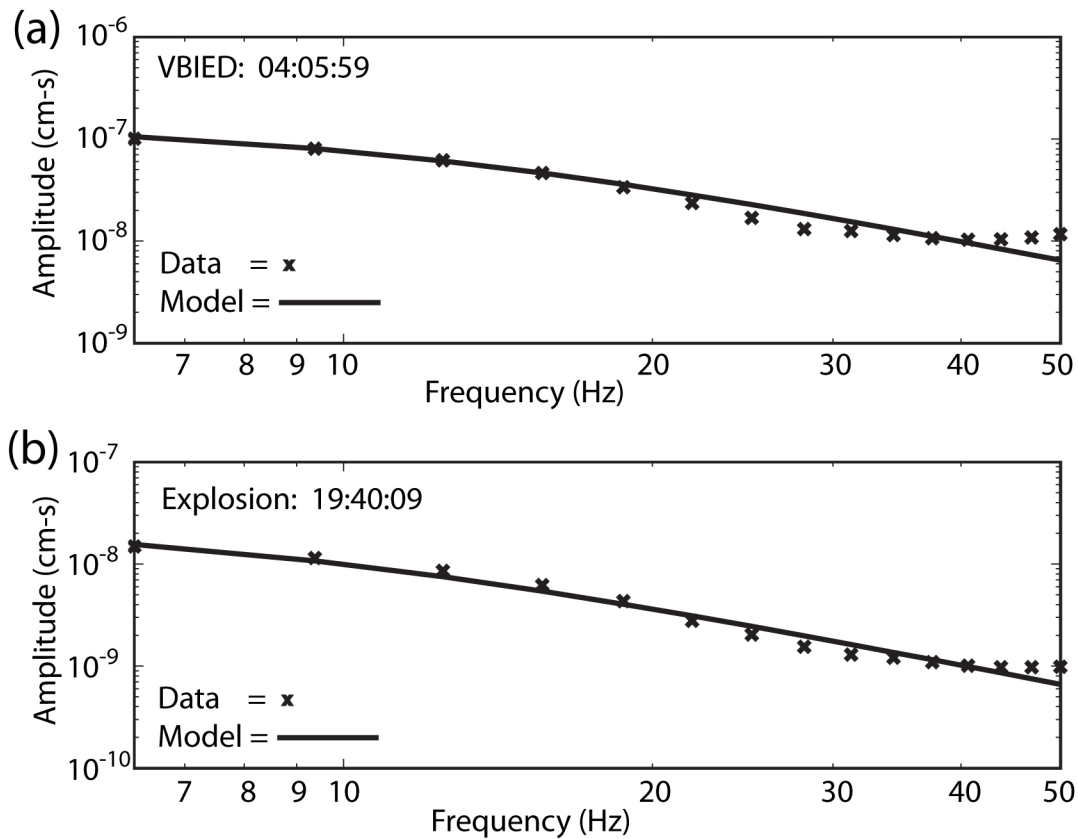


Figure 17. (a) Example of vertical-component displacement amplitude spectra for both a VBIED explosion at 04:06 UTC on 10 October 2006 (crosses), and the best fitting spectral model (solid line). (b) Similar example for the large ammunition explosion at 19:40 UTC, 10 October 2006.

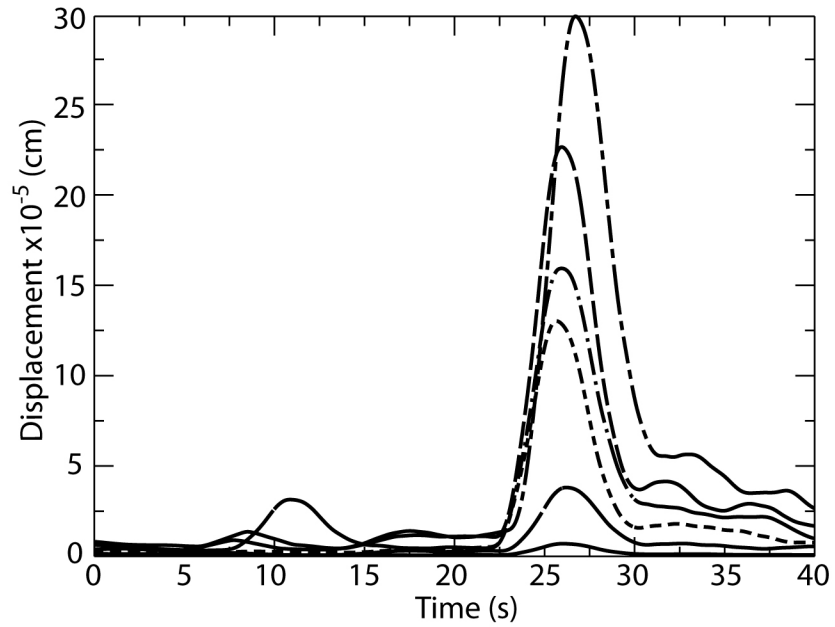


Figure 18. Smoothed envelope functions for 6 different explosions of differing sizes, displayed at the frequency band-pass of 4-8 Hz.

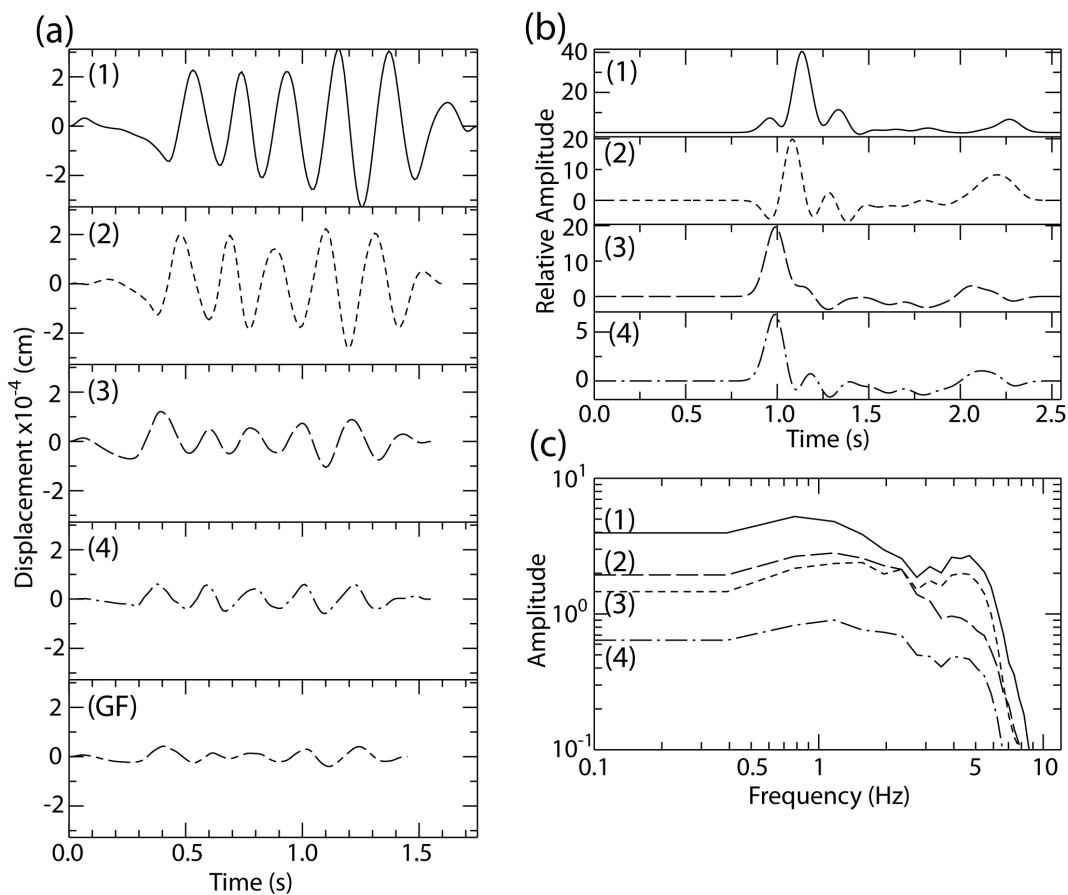


Figure 19. (a) Vertical-component seismograms of airwaves from 5 different explosions (details are given in Table 1). Seismograms are sorted by amplitude. The smallest signal (bottom) is selected as an empirical Green's function. (b) Estimated source-time functions for the the 4 explosions in (a) obtained by deconvolving out the Green's function. Because all of the source-time functions in (b) involve a small, wide pulse ~ 1.9 s after the main pulse, it is likely that this signal is not present in the assumed Green's function (bottom). (c) Amplitude spectra of the four source-time functions show difference in energy is at maximum at the low frequency region. At the higher frequencies above 5 Hz the difference is less because of the rapid high-frequency attenuation.